Available online at www.sciencedirect.com
SCIENCE DIRECT®
Journal of Photochemistry and Photobiology A: Chemistry 158 (2003) 145–162
Journal of Photochemistry and Photobiology A:Chemistry
www.elsevier.com/locate/jphotochem

Direct water splitting into H_2 and O_2 under visible light irradiation with a new series of mixed oxide semiconductor photocatalysts

Zhigang Zou, Hironori Arakawa*

Photoreaction Control Research Center (PCRC), National Institute of Advanced Industrial Science and Technology (AIST), 1-1-1 Higashi, Tsukuba, Ibaraki 305-8565, Japan

Received 5 July 2002; received in revised form 30 September 2002; accepted 7 October 2002

Abstract

The research on a new series of solid photocatalysts with different crystal structures was reviewed. The first system is $A_2B_2O_7$ pyrochlore-crystal type: Bi_2MNbO_7 (M = Al, Ga, In and Y, rare earth, and Fe), which is cubic system and space group Fd3m. The second system is ABO_4 stibotantalite-crystal type: $BiMO_4$ (M = Nb^{5+}, Ta^{5+}), in which both the triclinic system with space group P1 in the case of M = Ta and the orthorhombic system with space group Pnna in the case of M = Nb. The third system is ABO_4 wolframite-crystal type: $InMO_4$ (M = Nb^{5+}, Ta^{5+}), which is monoclinic system and space group P2/a. Although these photocatalysts crystallize in the different crystal structure, they contain the same octahedral TaO_6 and/or NbO_6 in the different photocatalysts. The band structure of the photocatalysts is defined by Ta/Nb d-level for a conduction band and O 2p-level for a valence band. The band gaps of the photocatalysts were estimated to be between 2.7 and 2.4 eV. Metal doped $InTaO_4$ photocatalysts were also investigated. Under visible light ($\lambda > 420$ nm) or ultra-violet irradiation, the H_2 and/or O_2 evolutions were observed from pure water as well as aqueous CH_3OH/H_2O and $AgNO_3$ solutions. The photocatalytic activity increases significantly by loading co-catalysts such as Pt, RuO_2 and NiO_x on the surface of the photocatalysts. Finally, direct water splitting into H_2 and O_2 under visible light irradiation was firstly established using newly synthesized NiO_x (partly oxidized nickel) promoted $In_{0.9}Ni_{0.1}TaO_4$ photocatalyst.

Keywords: Photocatalyst; Visible light irradiation; Water splitting

1. Introduction

Solar hydrogen production combines several attractive features for energy utilization. The photocatalytic water splitting into hydrogen and oxygen using oxide semiconductors under visible light irradiation has received much attention because the attempt aims at not only the direct production of hydrogen, a clean-energy, from water utilizing solar energy, but also the construction of artificial photosynthetic process as green plants are carrying out [1–10]. This renewable energy process utilizes absorption and conversion of solar energy, to split water and generate a hydrogen fuel. Extensive studies have been performed to split water under light irradiation [11–15], but the number of photocatalyst materials known up to now is yet limited, and the activity is still low. Therefore, it is in an urgent need to develop new type of photocatalyst materials with higher activity.

Recently, we have reported an evidence that photocatalytic water splitting is possible under visible light using a oxide semiconductor photocatalysts and the photocatalytic splitting of water may occur more effectively when suitable band gap is irradiated [16]. In order to improve photocatalytic activity, we investigated the effect of substitution in these photocatalysts for 3d-metal ions. Here, we report the review article of our recent research on three systems of solid photocatalysts with different crystal structure. To help understanding more about the origin of the photocatalysts, we also report the details of the characteristics of the photocatalysts such as crystal and band structures, as well as effect of co-catalysts on photocatalytic activity.

2. Experimental

The polycrystalline samples of the photocatalysts were synthesized by a solid-state reaction method. The pre-dried oxides with purity of 99.99% were used as starting materials. The stoichiometric amounts of starting materials were mixed and pressed into small columns. The columns were calcined and reacted in an aluminum crucible in air. This

* Corresponding author. Tel.: +81-298-61-4410; fax: +81-298-61-4750.
E-mail address: h.arakawa@aist.go.jp (H. Arakawa).

1010-6030/03/$ – see front matter © 2003 Elsevier Science B.V. All rights reserved.
doi:10.1016/S1010-6030(03)00029-7

process was repeated for three times. At the final process, the column samples were calcined and reacted for 2 days at 1100 °C. The chemical composition of the samples was determined by scanning electron microscope–X-ray energy dispersion spectrum (SEM–EDS) with accelerating voltage of 25 kV. The composition content was determined using the ZAF (Z: element number ("Z" number) correction; A: absorption correction; F: fluorescence correction) quantitative analysis program of SEM–EDS apparatus. Oxygen content was calculated from the EDS results [17]. The SEM–EDS analysis showed that the photocatalysts have a homogenous atomic distribution with no other additional elements. The chemical composition of these samples was confirmed to be the same before and after photocatalytic reaction. In order to obtain high photocatalytic activity, it is essential to load a metal or metal oxide as co-catalysts on the surface of photocatalyst [18]. The Pt particle was found to be the most effective for TiO_2 photocatalyst [18]. We loaded Pt particle onto the catalyst surface from aqueous methanol H_2PtCl_6 solution by an in situ photodeposition method. In other case, we loaded 1 wt.% partly oxidized nickel or RuO_2 onto the oxide semiconductor surface from aqueous $Ni(NO_3)_2$ or $RuCl_3$ solution by an impregnation method. The Ni-loaded photocatalysts were firstly calcined at 350 °C for 1 h in air and reduced in H_2 atmosphere at 500 °C for 2 h, then, treated in air atmosphere at 200 °C for 1 h. The double-layered structure of metallic Ni and NiO (denoted NiO_x) was formed on the surface of photocatalyst by the reduction–oxidation procedure. The Ru-loaded photocatalysts were calcined at 500 °C for 2 h in air.

The crystal structure was determined by powder X-ray diffraction method using Cu Kα radiation (λ = 1.54178 Å). The surface area was determined by BET measurement (Micrometritics, Shimadzu, Flow Prep 060, Japan). Photocatalytic reaction was carried out using the reaction cell connected to a closed gas circulation system. The gases evolved were determined with TCD gas chromatograph, which was connected to a gas circulating line. The photocatalytic reaction under UV irradiation was conducted using an inner-irradiation type quartz cell with 400 W high-pressure Hg lamp. The photocatalytic reaction under visible light irradiation was conducted using a Pyrex glass cell and 300 W Xe lamp. The 420 nm cut filter was placed onto the window face of the Pyrex glass cell.

3. Results and discussion

3.1. Bi_2MNbO_7 (M = Al, Ga, In and Y, rare earth and Fe) system

It is known that a number of compounds with the $A_2^{3+}B_2^{4+}O_7$ pyrochlore structure exhibit antiferroelectric phases or dielectric anomalies, only a few compounds exhibit a ferroelectric behavior. Bi_2MNbO_7 belongs to the family of the $A_2B_2O_7$ compounds, but space group and lattice constants are not yet clear. On the other hand, no photophysical property of the Bi_2MNbO_7 compound has been reported so far. We considered that M^{3+} and Nb^{5+} doping of B_2 site in $A_2^{3+}B_2^{4+}O_7$ might cause an increase in hole (carrier) concentration, and might provide a change in the magnetic, electrical transport, photophysical and photocatalytic properties.

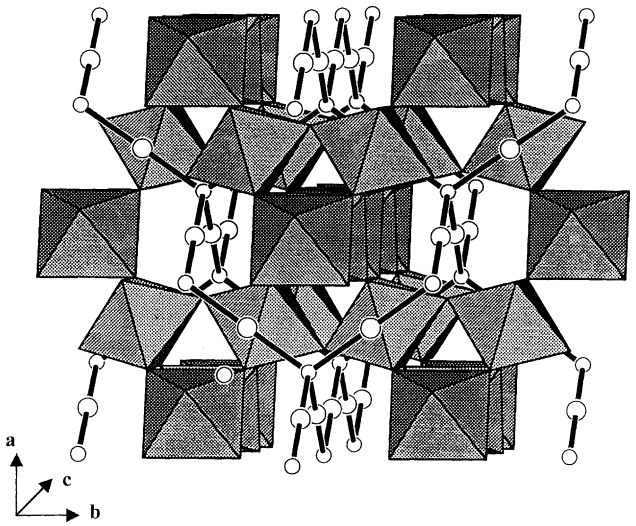

Fig. 1. The schematic structural diagram of Bi_2MNbO_7 (M = Al, Ga, In and Y, rare earth). Three-dimensional network of MO_6 stacked along [0 0 1] and separated by a unit cell translation.

Fig. 1 shows the crystal structure of the Bi_2MNbO_7 photocatalyst with $A_2B_2O_7$ pyrochlore-crystal type. The structure consists of the three-dimensional network of octahedral MO_6 (M = Al, Ga, In, Y, rare earth, Fe and Nb). The octahedral MO_6 is connected each other into chains and the Bi ions are located in between octahedral MO_6. The detailed investigations on structure found that the three-dimensional network of octahedral MO_6 was stacked along [0 0 1]. This is consistent with the relatively smaller resistivity in this direction from conductivity measurement.

3.1.1. Bi_2MNbO_7 (M = Al, Ga, In)

The result of conductivity measurement on Bi_2InNbO_7 showed that electron–hole pairs in Bi_2InNbO_7 can move easily in this direction [19]. Fig. 2 shows the electrical resistivity of the Bi_2InNbO_7 compound in temperature range 250–650 K. The resistivity increases with decreasing temperature, indicating semiconducting behavior. The resistivity exhibits sudden increase when temperature decreases to about 350 K. The structure of Bi_2InNbO_7 is built by forming infinite corner-sharing MO_6 octahedra which formed $[MO_3]_\infty$ chains [38]. This suggests that charge carriers in Bi_2InNbO_7 can move easily in this direction. The large magnitude of the resistivity may be attributed to a boundary effect of crystalline grains since the present study was carried out using polycrystalline sample. The mobility of electron–hole pairs affects the photocatalysis because it affects the probability of electrons and holes to reach

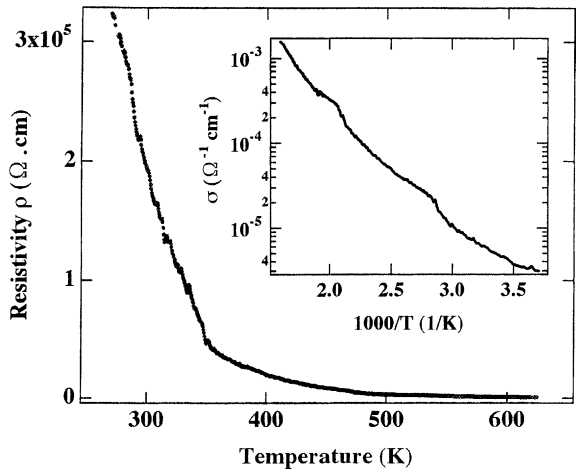

Fig. 2. Temperature dependence of the electrical resistivity of Bi_2InNbO_7. Inset: temperature dependence of the conductivity of Bi_2InNbO_7 in temperature range of 250–650 K.

reaction sites on the surface of photocatalyst [7,9,56,57]. This suggests that although the photocatalysts have a similar structure, the movement of electrons may be different.

We considered that a change of M^{3+} ionic radius in Bi_2MNbO_7 might cause a slight modification of crystal structure, resulting in delocalization of the charge carriers. The improvement in mobility of the charge is important to photocatalysts. Fig. 3 shows the result of UV-visible diffuse reflectance spectra of Bi_2MNbO_7 (M^{3+} = Al^{3+}, Ga^{3+}, In^{3+}). The onset of diffuse reflectance spectra of these photocatalysts showed an obvious shift to lower wavelength with decrease of the M^{3+} ionic radius. The value of band gaps of Bi_2MNbO_7 (M^{3+} = Al^{3+}, Ga^{3+}, In^{3+}) was estimated from plots of the square root of Kubelka–Munk functions $F(R)$ vs. photon energy [20]. The band gaps of the Bi_2MNbO_7 (M^{3+} = Al^{3+}, Ga^{3+}, In^{3+}) photocatalysts were estimated to be about 2.9, 2.75 and 2.7 eV from onset of diffuse reflectance spectra, respectively. The conductivity

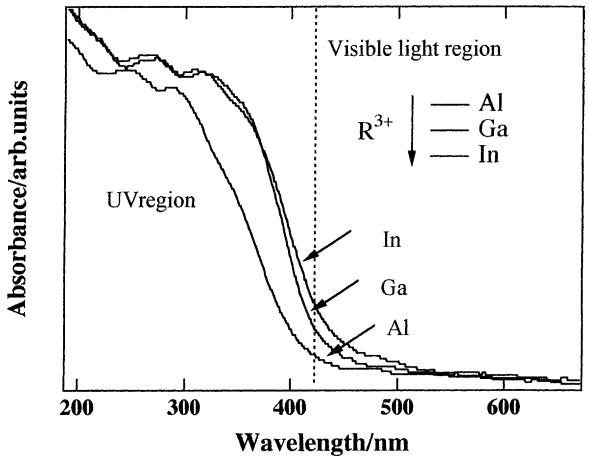

Fig. 3. UV-visible diffuse reflectance spectra on Bi_2MNbO_7 (M = Al, Ga and In) at room temperature. Samples were synthesized by a solid-state reaction at 1100 °C. R^{3+} denotes ionic radius of M.

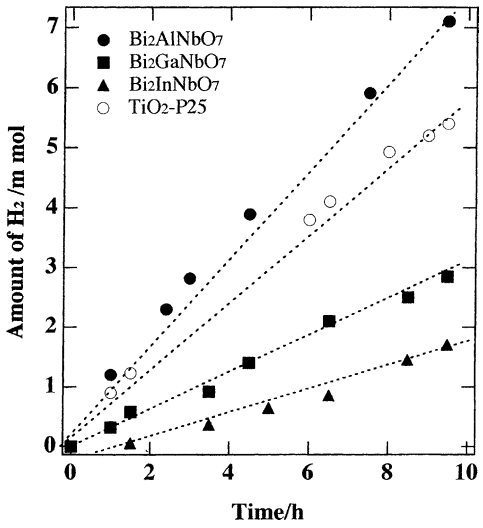

Fig. 4. Photocatalytic H_2 evolution on Pt/Bi_2MNbO_7 (M = Al, Ga, In) and Pt/TiO_2 from CH_3OH/H_2O solution. Cat.: 1 g, CH_3OH: 50 ml, H_2O: 350 ml, 400 W high-pressure Hg lamp.

of Bi_2InNbO_7 decreases rapidly with decreasing temperature (see Fig. 2). The activation energy (E_a) is 2.62(5) eV, according to function of $\sigma = \sigma_0 \exp(E_a/KT)$, where σ is the conductivity of the Bi_2InNbO_7 compound. The activation energy is in good agreement with the value (2.7 eV) estimated from UV-visible diffuse reflectance spectrum measurement. This means the Bi_2InNbO_7 compound may be a direct gap semiconductor. Furthermore, value of band gap of Bi_2MNbO_7 suggests that the compound has ability to generate H_2 evolution from water under visible light irradiation. However, these compounds did not split pure water directly under visible light.

Fig. 4 shows the H_2 evolution from CH_3OH/H_2O solution under UV irradiation with the Bi_2MNbO_7 (M = Al, Ga, In) photocatalysts. The CO evolution was also observed as the oxidation product in this reaction. The CO is formed by decomposition of the formaldehyde, which decomposes slower than methanol dehydrogenation. On the other hand, the ratios of non-stationary and non-stoichiometric evolutions between H_2 and CO might result from generation of CO_2 and other evolutions. It is well known that when CH_3OH is added to a Pt/TiO_2 aqueous suspension, sustained H_2 production is observed under UV irradiation and the alcohol molecules are oxidized to final productions of CO_2, CO, CH_4 and etc. [9]. The presence of oxygen vacancy defects strongly enhances such interaction due to electron back-donation from surface Ti^{3+} into π^* orbital of molecular CO [9]. The formation rate of H_2 increased rapidly with decrease of the M^{3+} ionic radii, Al^{3+} (0.57 Å) < Ga^{3+} (0.62 Å) < In^{3+} (0.92 Å). This means that the activity of these photocatalysts increases with decrease of M^{3+} ionic radii. The formation rate of H_2 evolution was estimated to be 0.71, 0.3, and 0.18 mmol g^{-1} h^{-1} in the first 10 h for Al^{3+}, Ga^{3+} and In^{3+}, respectively. It is notable that the formation rate of H_2 evolution with Bi_2AlNbO_7 is much larger

than that of TiO_2 photocatalyst (TiO_2-P25). This means that the activity of Bi_2AlNbO_7 to decompose CH_3OH/H_2O solution is higher than that of TiO_2 photocatalyst.

Although these photocatalysts did not work under visible light irradiation ($\lambda > 420$ nm) in our experiment, it is possible to modify the catalyst surface further for increasing the absorption range of wavelengths at which the catalyst is active. BET measurement showed that the surface areas of Bi_2MNbO_7 ($M = Al^{3+}$, Ga^{3+}, In^{3+}) are 0.51, 0.52 and 0.51 $m^2\,g^{-1}$, respectively. Since the surface area of these photocatalysts is only about 1% of that of the TiO_2 photocatalyst, it demonstrates the much higher efficiency of the new photocatalysts. It is evident that further increase in activity might be expected from increasing the surface area.

O_2 evolution reaction was performed in an aqueous cerium sulfate tetrahydrate solution and the following stoichiometric reaction occurred only: $4Ce_4{}^+ + 2H_2O \rightarrow 4Ce_3{}^+ + O_2 + 4H^+$. The aqueous $Ce(SO_4)_2$ solution is more stable than an aqueous silver nitrate under UV irradiation since photodeposition of $Ce_4{}^+$ did not occur after illumination. 11) However, the reaction, $2NO_3{}^- \rightarrow 2NO_2{}^- + O_2$, might occur in an aqueous $AgNO_3$ solution under UV irradiation since $NO_3{}^-$ is unstable, excepting the reaction, $4Ag^+ + 2H_2O \rightarrow 4AgO + O_2 + 4H^+$ [23–25]. The rate of O_2 evolution in the first 10 h increased rapidly with decrease of $M_3{}^+$ ionic radii.

Fig. 5 shows the H_2 evolution from pure water by Bi_2MNbO_7 powder photocatalysts under UV irradiation. The formation rate of H_2 evolution was about 1.5 μmol h^{-1} in the first 10 h with Bi_2InNbO_7. The total volume of evolved H_2 was attained to 40 μmol/catalyst (g) when this reaction achieved 50 h. TiO_2 photocatalyst (TiO_2-P25) was tested by the same method. The formation rate of H_2 evolution was about 0.7 μmol h^{-1} in the first 10 h. It is interesting to notice that the TiO_2 photocatalyst shows lower activity than that of Bi_2InNbO_7. Although the photocatalytic activity of TiO_2 photocatalyst is very high compared with Bi_2InNbO_7 under UV light irradiation in CH_3OH/H_2O solution, photocatalytic activity of TiO_2 is smaller than that of Bi_2InNbO_7 in pure water.

Oxygen evolution was not observed from pure water in this experiment using both Bi_2MNbO_7 and TiO_2. It is commonly accepted that free holes in TiO_2 particles can generate OH radicals either on the surface or even at the aqueous interface [41,42]. Extensive research found that there are both physisorbed and chemisorbed oxygen molecules in TiO_2 surface by low-energy photon irradiation [43,44]. The physisorbed O_2 molecules are produced through the neutralization of chemisorbed $O_2{}^-$ species by photogenerated holes [32,33]. Amy et al. [45] also found the similar result that the produced oxygen can be photoadsorbed on the surface of TiO_2 photocatalyst. Recently, Ishibashi et al. found that $O_2{}^-$ was formed on the order of 10^{14} cm^{-2} at the TiO_2 surface during photocatalytic reaction under UV light irradiation. This indicates photogenerated electron is mainly trapped by adsorbed oxygen resulting in the formation of $O_2{}^-$ [46]. The photoadsorption of oxygen over Bi_2InNbO_7 after pure water splitting reaction was investigated by measurement of magnetic susceptibility (χ). The result is shown in Fig. 6. The magnetic susceptibility of oxygen adsorbed on solid surface was studied by many researchers and it showed that adsorbed oxygen undergoes an antiferromagnetic transition around 50 K [35,47,48]. The susceptibility is different between two samples before and after reactions. The sample after reaction shows an obvious broad peak around 50 K. However, the sample before reaction does not have any anomaly around 50 K. Measurements under zero field and field cooled conditions revealed that the susceptibility is independent to the applied magnetic field. This fact suggests that the origin of this anomaly is unlikely from a

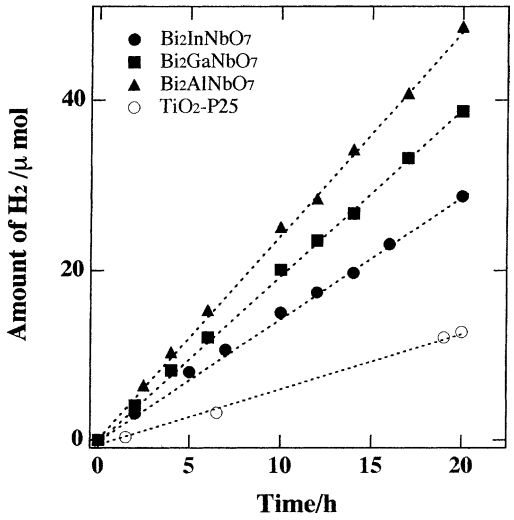

Fig. 5. Photocatalytic H_2 evolution on Pt/Bi_2MNbO_7 ($M^{3+} = Al^{3+}$, Ga^{3+}, In^{3+}) and Pt/TiO_2 (P25) from pure water. Cat.: 1 g, H_2O: 400 ml, 400 W high-pressure Hg lamp.

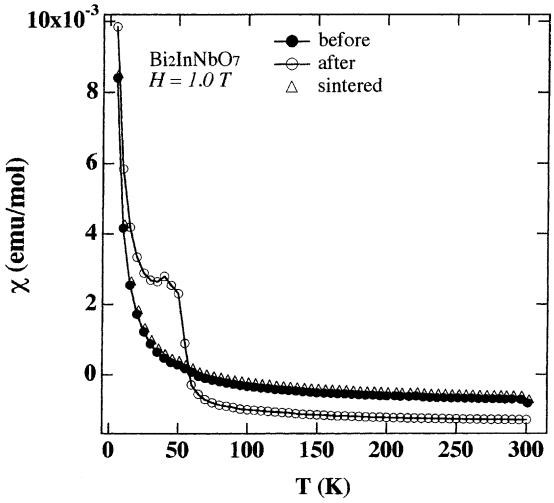

Fig. 6. Temperature dependence of magnetic susceptibilities of samples before and after reactions.

spin-glass-like behavior. To understand further the origin of this anomaly, the sample after reaction was sintered at 600 °C using an electric furnace to deoxidation. The sintered sample showed the same result as that of sample before reaction (see Fig. 6), the broad peak around 50 K was disappeared after sintering. The anomaly seen around 50 K might arises from the antiferromagnetic ordering of adsorbed oxygen in the sample. The similar result was also observed in other compounds containing niobium, such as $K_7Nb_{14.13}P_{8.87}O_{60}$ and $BaNb_2S_5$ [49,50]. Although it is not clear whether the O_2 molecule photoadsobed on surface of the photocatalysts is physisorbed or chemisorbed molecule states, we speculate that the phenomenon takes place on the surface of our photocatalysts.

3.1.2. Bi_2MNbO_7 (M = Y and rare earth) system

In order to determine the effect of ion size on the band structure and photocatalytic activity of oxide semiconductors, we have chosen Bi_2RNbO_7 (R = Y, rare earth) system [58]. In the rare earth compounds, the strongly localized f-shell, that is considered usually as a core-like shell, determines the similar chemical and physical properties of the lanthanides [29,30]. The variation of their properties across the lanthanides often has a monotonic character. Fig. 7 shows the UV-visible diffuse reflectance spectra of all these compounds. The spectra show an obvious change with different R ions. The onset of UV-visible diffuse reflectance spectra shifts to shorter wavelength with increase of the R ion radius $r_R{}^{3+}$, except for R = Ce. It is well known that cerium has both Ce^{3+} and Ce^{4+}. The cerium is generally a mixture of Ce^{4+} and Ce^{3+} in Ce compounds. The $r_{Ce}{}^{3+}$ is $>r_Y{}^{3+}$; ($r_Y{}^{3+} < \cdots < r_{Pr}{}^{3+} < r_{Ce}{}^{3+} < r_{La}{}^{3+}$), while the $r_{Ce}{}^{4+}$ is $<r_Y{}^{3+}$; ($r_{Ce}{}^{4+} < r_Y{}^{3+} < \cdots < r_{La}{}^{3+}$). The Ce compound showed a clear absorption edge at around 580 nm,

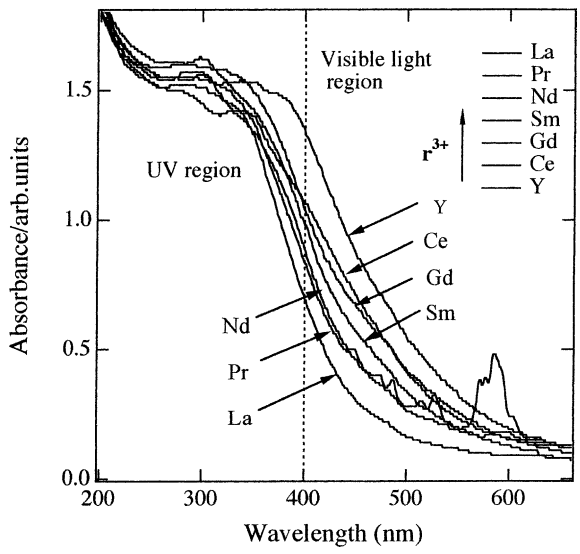

Fig. 7. UV-visible diffuse reflection spectra on Bi_2RNbO_7 (R = Y, rare earth) at room temperature. Samples were synthesized by a solid-state reaction at 1100 °C. r^{3+} denotes ionic radius of R.

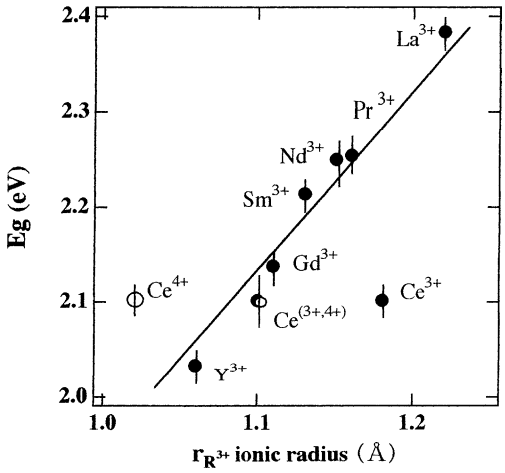

Fig. 8. Band gaps E_g as a function of the R ion radius $r_R{}^{3+}$ in Bi_2RNbO_7 (R = Y, rare earth). The band gap was estimated from plots of the square root of Kubelka–Munk functions $F(R)$ vs. photon energy.

which is close to that of CeO_2. Assuming that the cerium in Bi_2RNbO_7 is a mixture of Ce^{4+} and Ce^{3+}, the absorption edges of these compounds shift to shorter wavelength with increase of the R ion radius $r_R{}^{3+}$.

It should be noted that the onset of the absorption edges of Bi_2RNbO_7 (R = Pr and Nd) became unclear because several absorptions overlap in the range 450–650 nm. These phenomena can be attributed to internal transitions in a partly filled 4f-shell. Actually, the spectra in this region are in accord with those observed in rare earth hexahalide complexes and simple sesquioxides. The band gap of these compounds can be estimated from plots of the square root of Kubelka–Munk functions $F(R)$ vs. photon energy [20]. Fig. 8 shows the estimated band gaps of all compounds. The band gaps of Bi_2RNbO_7 are in the range from 2 to 2.4 eV. Band gap E_g is linearly dependent on R ion radius, $r_R{}^{3+}$, assuming that the cerium is a mixture of Ce^{4+} and Ce^{3+}. This means that it is possible to construct the dependence of $E_g = f(r_R{}^{3+})$ for these oxide semiconductors. One of the most characteristic features is that E_g increases with increasing $r_R{}^{3+}$. It is interesting to notice that the photocatalysts have ability to respond wavelength of visible light region.

Fig. 9 shows the photocatalytic activity, $A_R{}^{3+}$ ($A_R{}^{3+}$ is efficient evolution of H_2 from pure water under UV irradiation, $H_2/\mu mol\,h^{-1}$), as a function of the R ion radius, $r_R{}^{3+}$, in Bi_2RNbO_7. The $A_R{}^{3+}$ decreases with increasing $r_R{}^{3+}$. The results are in good agreement with the observed absorption spectra and band characteristics of all these photocatalysts as shown in Figs. 7 and 8. This is considered largely to be a consequence of the R-4f levels, which form the narrower band with the smaller R ion radius $r_R{}^{3+}$. Since the narrower band gap suggests easier excitation for an electron from the valence band to the conduction band in oxide semiconductor, this results in higher photocatalytic activity. This difference in R-4f levels and the corresponding difference in the band gaps lead to different photocatalytic behavior. Also, it is

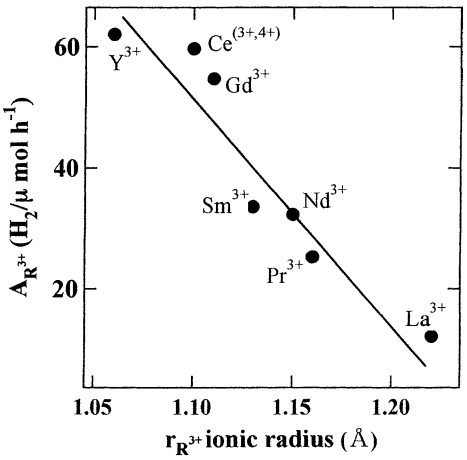

Fig. 9. Photocatalytic activity $A_R{}^{3+}$ as a function of the R ion radius $r_R{}^{3+}$ in non-promoted Bi_2RNbO_7 (R = Y, rare earth). A_R is efficient evolution of H_2 from pure water under UV irradiation. Cat.: 1 g, H_2O: 400 ml, 400 W high-pressure Hg lamp.

evident that the different photocatalysts used here have very similar surface areas; hence the differences in photocatalytic activity cannot be attributed to variations in surface area.

3.1.3. Bi_2MNbO_7 (M = 3d-Fe) system

We also investigated the effect of substitution in $A_2{}^{3+}B_2{}^{4+}O_7$ pyrochlore structure for 3d-metal ions [59,60]. We suggest that substitution of In^{3+} by 3d-Fe^{3+} in Bi_2InNbO_7 might cause a slight modification of crystal structure, resulting in a change in photocatalytic and photophysical properties. The change of lattice constants might lead to hole/electron delocalization. However, the improvement in mobility of the charge is important to photocatalysts because it affects the probability of electrons to reach reaction sites on the surface of photocatalyst.

Fig. 10 shows the UV-visible diffuse reflectance spectra of both Bi_2FeNbO_7 and Bi_2InNbO_7. The onset of spectra of these photocatalysts showed an obvious shift to longer wavelength with In^{3+} being substituted by 3d-Fe^{3+}. The band gaps of the Bi_2MNbO_7 (M^{3+} = Fe^{3+} and In^{3+}) photocatalysts were estimated to be about 2.2 and 2.7 eV from onset of diffuse reflectance spectra. This means that the band gap decreases with substitution of In^{3+} by 3d-Fe^{3+} in Bi_2InNbO_7.

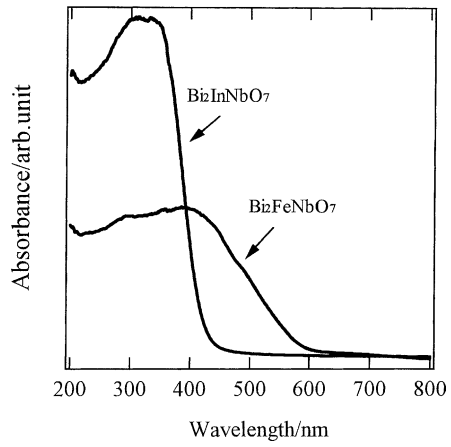

Fig. 10. UV-visible diffuse reflectance spectra of Bi_2MNbO_7 (M^{3+} = Fe^{3+}, In^{3+}).

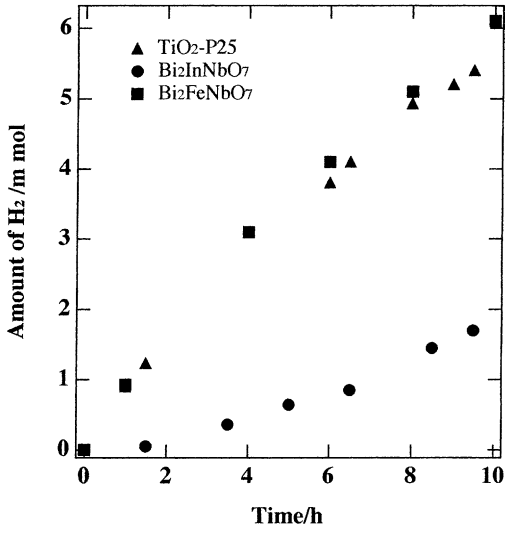

Fig. 11. Photocatalytic H_2 evolution over Pt/Bi_2MNbO_7 (M^{3+} = Fe^{3+}, In^{3+}) and Pt/TiO_2 (P25) from CH_3OH/H_2O solution under UV irradiation. Cat.: 1 g, CH_3OH: 50 ml, H_2O: 350 ml, 400 W high-pressure Hg lamp.

Fig. 11 shows the H_2 evolution from CH_3OH/H_2O solution under UV irradiation with the Bi_2MNbO_7 (M^{3+} = Fe^{3+}, In^{3+}) photocatalysts. The formation rate of H_2 increased significantly with In^{3+} being substituted by 3d-Fe^{3+} and it was estimated to be 0.6 and 0.18 mmol g^{-1} h^{-1} during the first 10 h, respectively. The total amount of H_2/catalyst (mol) for these compounds was much greater than 1 after 10 h, indicating that the reaction occurs catalytically. The reaction stopped when the UV light was turned off in this experiment, showing the obvious light response. It is notable that the formation rate of H_2 evolution for Pt/Bi_2FeNbO_7 is slightly large than that of Pt/TiO_2 photocatalyst (TiO_2-P25). The CO evolutions were also observed in this reaction from CH_3OH/H_2O solution as the oxidation product. Further, O_2 evolution reaction was performed in an aqueous cerium sulfate solution and the following stoichiometric reaction took place:

$$4Ce^{4+} + 2H_2O \rightarrow 4Ce^{3+} + O_2 + 4H^+$$

The formation rate of O_2 evolutions in the first 5 h increased rapidly with decrease of M^{3+} ionic radii in a similar manner as H_2 evolution. This means that the photocatalysts have potentials for O_2 evolution from aqueous solution and the potential activity for O_2 evolutions increase with decrease of M^{3+} ionic radii. It is interesting to notice that the formation rate of O_2 evolution on Bi_2FeNbO_7 is much larger than that on the TiO_2 photocatalyst. This means that the activity of Bi_2FeNbO_7 is much higher than that of the TiO_2 photocatalyst.

The detailed investigations on structure found that the three-dimensional network of octahedral MO_6 ($M = Fe^{3+}$, In^{3+} and Nb^{5+}) in crystal structure of Bi_2MNbO_7 ($M^{3+} = Fe^{3+}$, In^{3+}) are stacked along [0 0 1]. The mobility of electron–hole pairs affects the photocatalysis because it affects the probability of electrons and holes to reach reaction sites on the surface of photocatalyst. This suggests that although both Bi_2FeNbO_7 and Bi_2InNbO_7 have similar structure, the movement of electrons might be more easily in Bi_2FeNbO_7 than that in Bi_2InNbO_7. The band structure of oxides is generally defined by M d-level and O 2p-level. Scaife [22] examined that the valence band energy should be assumed by the O 2p-levels in MO_6 and the conduction band should be assumed by d-levels in MO_6 when the compound contains octahedral MO_6. The band gaps of Bi_2MNbO_7 ($M^{3+} = Fe^{3+}$, In^{3+}) decreased from 2.7 eV for Bi_2InNbO_7 to 2.2 eV for Bi_2FeNbO_7 with In^{3+} being substituted by 3d-Fe^{3+}. The difference of band gaps in the photocatalysts might result from that of conduction band. The valence band potentials of the Bi_2MNbO_7 ($M^{3+} = Fe^{3+}$, In^{3+}) photocatalysts should be the same because they have same crystal structure. The conduction band potentials of the photocatalysts might be changed because the difference of octahedrons in the Bi_2MNbO_7 ($M^{3+} = Fe^{3+}$, In^{3+}) photocatalysts. The conduction bands of Bi_2MNbO_7 ($M^{3+} = Fe^{3+}$, In^{3+}) should be slightly changed towards positive with In^{3+} being substituted by Fe^{3+} since the band gaps of Bi_2MNbO_7 ($M^{3+} = Fe^{3+}$, In^{3+}) decrease with In^{3+} being substituted by 3d-Fe^{3+}.

It is known that the photooxidation/photodissolution of catalyst might consume oxygen. However, such a reaction generally leads to the changes in crystal structure and the chemical composition of photocatalyst. We examined the atomic ratio and the crystal structure of Bi_2MNbO_7 ($M^{3+} = Fe^{3+}$, In^{3+}) before and after photocatalytic reactions. From our experimental results we confirmed that these samples before and after reactions have not changed in both the crystal structure and the chemical composition. The difference in the surface area of the photocatalysts can generally lead to the difference in photocatalytic activity since an efficient photocatalytic reaction process occurs on the photocatalyst surface. However, Bi_2InNbO_7 and Bi_2FeNbO_7 have very similar surface area; hence the difference photocatalytic activity cannot be attributed to variations in surface area. This fact suggests the difference in the photocatalytic activity may be mainly due to their different band structure.

3.2. $BiMO_4$ ($M = Nb$, Ta) system

The niobates and tantalates consisting of NbO_6 or TaO_6 octahedron connected by sharing corners have long been of interest in the past because of their ferroelectric, optoelectronic and efficient luminescence properties [51–54]. Recently, we found that the compounds consisting of NbO_6 or TaO_6 octahedron could decompose water into H_2 and/or O_2 under UV or visible light irradiation

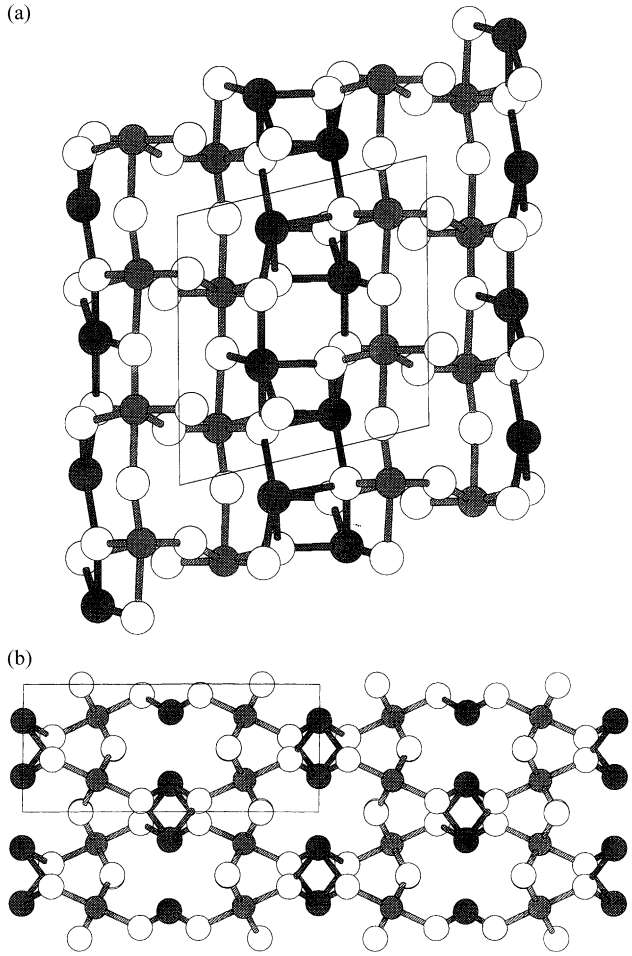

Fig. 12. The schematic structural diagram of the triclinic and orthorhombic $BiTa/NbO_4$ compounds: (a) the triclinic system; (b) the orthorhombic system.

[8,61,62]. $BiTaO_4$ and $BiNbO_4$ are known to crystallize in two forms, triclinic (high-temperature β-type) and orthorhombic (low-temperature α-type) system. The powder X-ray diffraction analysis showed that $BiTaO_4$ is triclinic system (high-temperature β-type) with space group P1 in our sample. However, $BiNbO_4$ is orthorhombic system (low-temperature α-type) with space group Pnna. Substitution effects of Ta^{5+} by Nb^{5+} in $BiTa_{1-x}Nb_xO_4$ ($0 \leq x \leq 1$) on photocatalytic, photophysical and structural properties were investigated. The structure of $BiTa_{1-x}Nb_xO_4$ at R = Nb/Bi = 0 and 0.5 is triclinic system with space group P1. However, the structure at R = 0.2, 0.8 and 1 is orthorhombic system with space group Pnna. Fig. 12 shows the schematic structural diagram of the triclinic and orthorhombic systems. Full-profile structure refinement of the collected powder diffraction data was performed using the Rietveld program REITAN [21]. For the triclinic system, the lattice parameter is $a = 7.6627(1)$ Å, $b = 5.5875(2)$ Å, $c = 7.7835(2)$ Å, $\alpha = 90.052(2)^\circ$, $\beta = 77.0282(2)^\circ$, $\gamma = 86.468(2)^\circ$. The triclinic structure can be described as consisting of puckered sheets of formula $[TaO_4]_\infty$. The

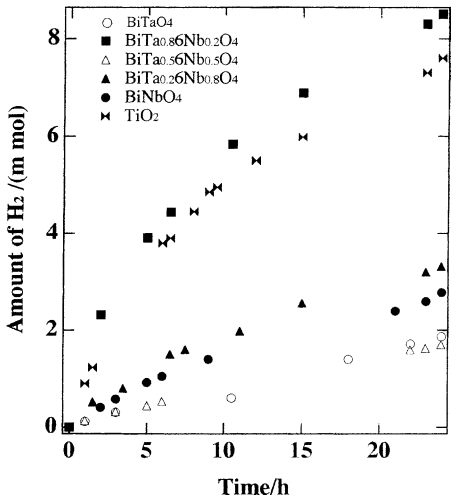

Fig. 13. H_2 evolution from CH_3OH/H_2O solution with $Pt/BiTa_{1-x}Nb_xO_4$ under UV irradiation. Cat.: 1 g, CH_3OH: 50 ml, H_2O: 350 ml, 400 W high-pressure Hg lamp.

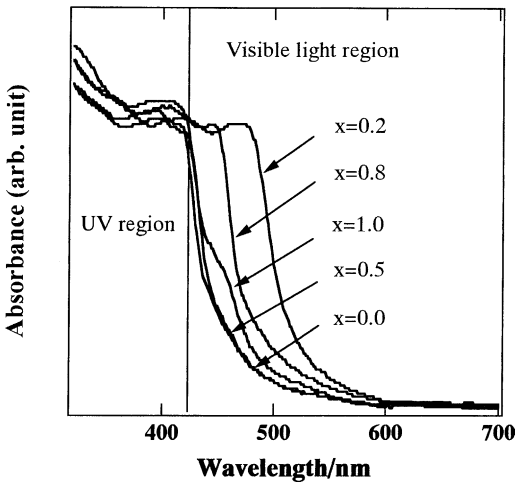

Fig. 14. UV-visible diffuse reflectance spectra of $BiTa_{1-x}Nb_xO_4$ ($0 \leq x \leq 1$) at room temperature.

Ta–O octahedra parallel to the *bc* plane and corners to four others join each octahedron and the sheets are held together by bismuth atoms. For the orthorhombic system, the lattice parameter is $a = 5.6821(1)$ Å, $b = 11.7160(2)$ Å, $c = 4.9844(1)$ Å. The orthorhombic structure can be described that both Bi and Nb have distorted octahedral oxygen coordination. The Nb–O octahedra are linked over four corners and thus the structure can be viewed as consisting of sheets of $[NbO_4]_\infty$ units separated by bismuth atoms.

Fig. 13 shows the H_2 evolution from CH_3OH/H_2O solution with $BiTa_{1-x}Nb_xO_4$ under UV irradiation. The reaction stopped when the light was turned off in this experiment, showing the obvious light response. The result shows that the photocatalytic reaction is induced by the absorption of UV irradiation. The rate of H_2 evolution with orthorhombic $BiTa_{1-x}Nb_xO_4$ at $x = 0.2$, 0.8 and 1 appeared much larger than that with triclinic $BiTa_{1-x}Nb_xO_4$ at $x = 0$ and 0.5. The $BiTa_{1-x}Nb_xO_4$ photocatalyst with orthorhombic structure has higher activity than that with triclinic structure. The orthorhombic $BiTa_{1-x}Nb_xO_4$ at $x = 0.2$ showed the highest activity. The rate of H_2 evolution was estimated to be 600 μmol h^{-1} in the first 10 h. The total amount of H_2/catalyst (mol) was beyond 1 at 2 h, indicating that the reaction occur catalytically. Total volume of evolved H_2 was 9000 μmol/catalyst (g) when this reaction was conducted for 24 h, the value corresponded to 4.3 mol ratio of H_2 evolution to catalyst.

The UV-visible diffuse reflectance spectra of the $BiTa_{1-x}Nb_xO_4$ photocatalysts are shown in Fig. 14. These spectra of triclinic $BiTa_{1-x}Nb_xO_4$ ($x = 0$ and 0.5) are almost the same, while those of orthorhombic $BiTa_{1-x}Nb_xO_4$ ($x = 0.2$, 0.8 and 1) show an obvious shift to shorter wavelength as x increases. The onset of diffuse reflectance spectra of the triclinic structure shows a shift to shorter wavelength than that of the orthorhombic structure. This is consistent with the observation of photocatalytic reaction in which the compounds with triclinic structure showed lower activity than those with orthorhombic structure (see Fig. 12(b)). The onset of diffuse reflectance spectrum shifted to longer wavelength means that the compound can utilize smaller irradiation light energy. The band gap of $BiTa_{1-x}Nb_xO_4$ at $x = 0$ and 0.5 was estimated to be about 2.7(4) eV. However, the band gaps of $BiTa_{1-x}Nb_xO_4$ at $x = 0.2$, 0.8 and 1 are 2.3(1), 2.5(2) and 2.6(4) eV, respectively. The study of the luminescent properties found that the luminescent properties of β-Bi(Nb/Ta)O_4 and α-Bi(Nb/Ta)O_4 are different since the crystal structure of the compounds are different [26]. However, all compounds showed broad excitation and emission bands, and have low quenching temperature. This turned out that it is contrary to the result of UV-visible diffuse reflectance spectra. It was explained that the $6s^2$ valence band levels of bismuth lie just above the 2p-O^{2-} valence band levels in β-phase, while $6s^2$ valence band levels of bismuth lie beneath the top of the 2p-O^{2-} in α-phase. As shown in Fig. 12, all the present compounds consist of the three-dimensional network of octahedral MO_6 (M = Nb and/or Ta). The octahedral MO_6 is connected to each other into chains and the Bi ions are located between octahedral MO_6. If $6s^2$ valence band levels of bismuth lie beneath the top of the 2p-O^{2-}, then the E_g would be determined by the gap between valence band O 2p-level and the conduction band Nb 4d-level in MO_6 of the compounds. In such cases, the E_g would be 3.64 eV due to the flat band potential of O 2p-level and Nb 4d-level are 2.94 (SHE) and −0.7 eV, respectively in the oxide semiconductors [22]. However, according to results of luminescence, the E_g should be 3.5 and 3.75 eV for β-$BiNbO_4$ and α-$BiNbO_4$, respectively. This fact suggests that luminescence properties are determined by 2p-4d/5d charge-transfer in both β- and α-$BiNbO_4$.

It is interesting to note that $BiTa_{1-x}Nb_xO_4$ absorbs the visible light ($\lambda > 420$ nm), but the absorption is weak. If $6s^2$ valence band levels of bismuth lie beneath the top

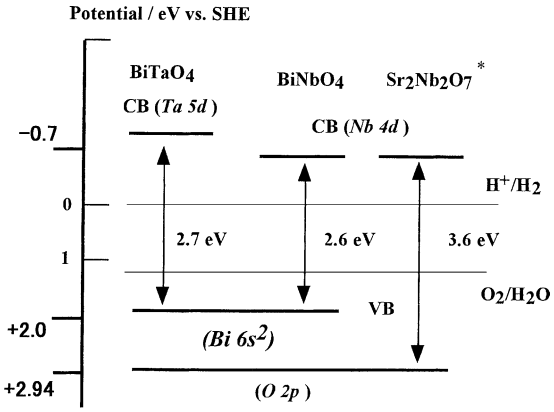

Fig. 15. The suggested band structures of both $BiTaO_4$ and $BiNbO_4$ synthesized by a solid-state reaction at 1100 °C.

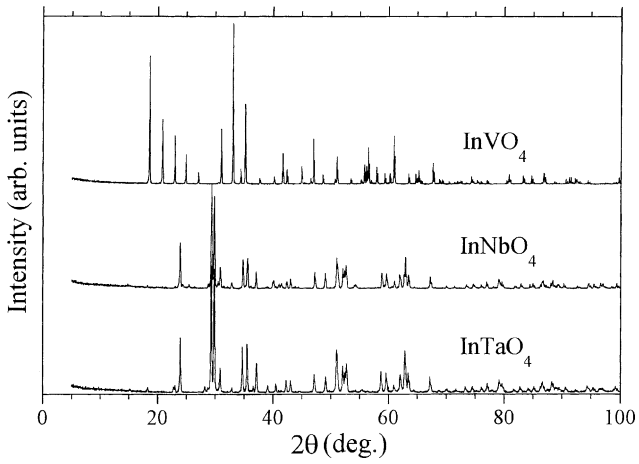

Fig. 16. X-ray powder diffraction patterns of the $InMO_4$ (M = V, Nb, Ta) photocatalysts.

of the 2p-O^{2-}, the characteristic absorption under visible light region is impossible. This fact suggests that Bi-$6s^2$ and Nb/Ta-4d/5d determines the band gap energy of the oxide semiconductors. The valence band potentials of both compounds should be the same because they contain Bi-$6s^2$. Fig. 15 shows the suggested band structures of the compounds. The valence band potentials of both compounds should be the same because they contain Bi-$6s^2$. The difference of band gaps might be resulted from that of the conduction band, coming from 5d of TaO_6 and 4d of NbO_6. This is consistent with the observation of photocatalytic activity, since the narrower band gap suggests easier excitation for an electron from the valence band to the conduction band in oxide semiconductor. However, some detailed experiments will be necessary for clarification of the mechanism.

Needless to say, knowledge of the band gap of these compounds is particularly important to their use in the systems of photocatalytic H_2 evolution. It should be noted that these photocatalysts can work only under UV light irradiation ($\lambda < 420$ nm) in the experiment. Alig et al. [31] have shown that direct absorption of photons by the band gap of oxides can generate electron–hole pairs in the solid. However, the energy requirement is generally higher than the band gap of the oxides. The effective way to make the present photocatalysts active under visible light irradiation ($\lambda > 420$ nm) would be to modify the catalyst surface further, such as loading other co-catalyst onto the catalyst surface.

3.3. $InMO_4$ (M = V, Nb, Ta) system

We extended our research from 5d metal Ta, 4d-metal Nb, to 3d-metal V, and succeeded in synthesizing new series of photocatalysts $InMO_4$ (M = V, Nb, Ta) [6,55,63,64]. The ionic radius of Ta^{5+} is almost the same as that of Nb^{5+}, which results in the presence of isostructural $InTaO_4$ and $InNbO_4$. However, $InVO_4$ shows different crystal structure from $InTaO_4$ and $InNbO_4$. The crystal structures of the $InMO_4$ (M = V, Nb, Ta) compounds were investigated by the powder X-ray diffraction method. Fig. 16 shows the X-ray powder diffraction patterns of the $InMO_4$ compounds. Those of the 5d and 4d-transition metal compounds, $InTaO_4$ and $InNbO_4$, appear very similar, but 3d-transition metal compound $InVO_4$ shows a totally different feature. The further investigations of structure revealed that the $InTaO_4$ and $InNbO_4$ compounds crystallize in the same wolframite-type structure, monoclinic system with space group of P2/a, lattice parameters $a = 5.1552(1)$ Å, $b = 5.7751(1)$ Å, $c = 4.8264(1)$ Å, $\beta = 91.373(1)°$ for $InTaO_4$ and $a = 5.1440(8)$ Å, $b = 5.7709(6)$ Å, $c = 4.8355(6)$ Å, $\beta = 91.13(1)°$ for $InNbO_4$. In contrast, the 3d-metal compound $InVO_4$ belongs to the orthorhombic system, space group Cmcm, $a = 5.765(4)$ Å, $b = 8.543(5)$ Å and $c = 6.592(4)$ Å. Fig. 17 shows the schematic structural diagrams of the $InTaO_4$, $InNbO_4$ and $InVO_4$ photocatalysts. In structure of $InTaO_4$ and $InNbO_4$, there are two kinds of octahedron, $NbO_6(TaO_6)$ and InO_6. The InO_6 octahedron connects to each others to form zigzag chains by sharing edges. These InO_6 chains are connected through $NbO_6(TaO_6)$ octahedron to form the three-dimensional network.

The $NbO_6(TaO_6)$ and InO_6 octahedrons form the layers by sharing the corner as shown in Fig. 17(a). Oxygen planes are formed in parallel with (0 0 1) plane. Although $InTaO_4$ and $InNbO_4$ show similar crystal structure, a change of lattices parameters along the all the axis was observed between $InTaO_4$ and $InNbO_4$. The volume of InO_6 octahedron seems to have little difference between $InTaO_4$ (13.601 $Å^3$) and $InNbO_4$ (13.607 $Å^3$). However, the volume of NbO_6 and TaO_6 expands slightly from 10.607 $Å^3$ in $InNbO_4$ to 10.648 $Å^3$ in $InTaO_4$. The expansion of the TaO_6 volume suggests leading to longer lattice parameters in $InTaO_4$. In $InVO_4$, the structure is composed of chains of the InO_6 octahedra linked together by the VO_4 tetrahedra [55].

Although the V, Nb and Ta transition metals are all belonging to the 5B group in the periodic table, the 5d metal Ta and 4d-metal Nb are often reported to form compounds with similar structures, while the 3d-transition metal V behaves

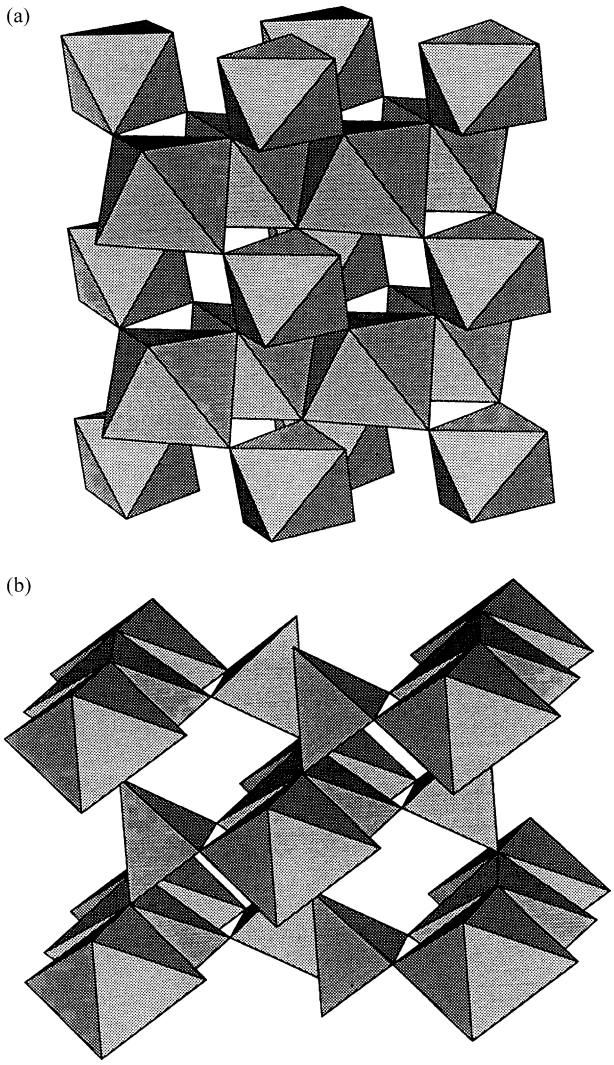

Fig. 17. Schematic structures of $InTaO_4$, $InNbO_4$ and $InVO_4$ [55]: (a) $InTaO_4$ and $InNbO_4$; (b) $InVO_4$.

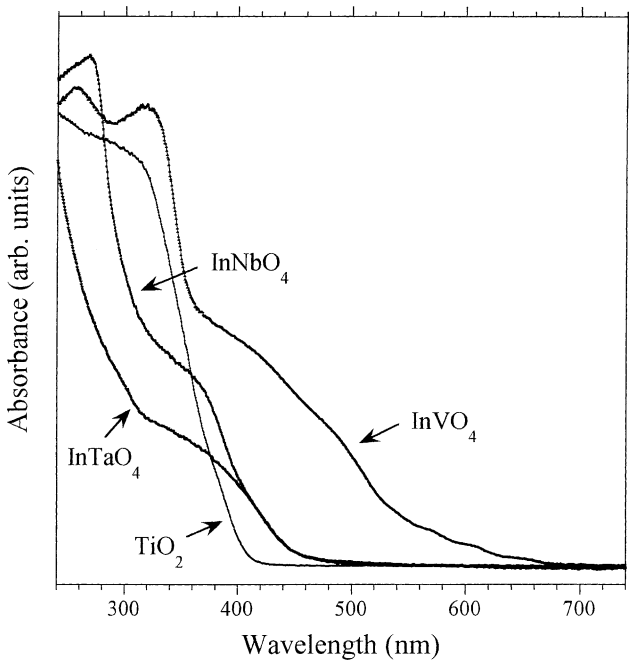

Fig. 18. UV-visible diffuse reflectance spectra of the $InVO_4$, $InNbO_4$ and $InTaO_4$ photocatalysts. As a comparison, spectrum of TiO_2 is shown together [55].

in a more complicated manner [55]. It is not surprising that the $InMO_4$ (M = V, Nb, Ta) compounds form in different structures and hence exhibit different physical and chemical properties. Fig. 18 shows the UV-visible diffuse reflectance spectra of the new photocatalysts. In contrast to the well known TiO_2 whose absorption edge is about 400 nm, all the three $InMO_4$ compounds showed absorption in visible light region. The visible light responding behavior becomes extremely clear in $InVO_4$, where the band gap was estimated to be 1.9 eV. The band gaps of $InTaO_4$ and $InNbO_4$ were estimated to be 2.6 and 2.5 eV from diffuse reflectance spectra. The small difference of band gaps between $InNbO_4$ and $InTaO_4$ might be resulted from that of the conduction band. This is consistent with the observation of photocatalytic activity. The difference between the conduction bands of $InNbO_4$ and $InTaO_4$, coming from 5d of TaO_6 and 4d of NbO_6, seems to lead to the difference of photocatalytic activity between $InNbO_4$ and $InTaO_4$. The potentials of conduction band of $InNbO_4$ and $InTaO_4$ are more negative than that of H_2 evolution, leading to H_2 evolution from pure water. The photocatalytic and photophysical properties of photocatalysts change with crystal structure. One of the most important key factors for $InTaO_4$ and $InNbO_4$ is that there are two kinds of octahedron, InO_6 and $NbO_6(TaO_6)$, in the crystal structure. The difference of volume between TaO_6 and NbO_6 leads to a change of the lattice parameters between $InTaO_4$ and $InNbO_4$. The difference of photocatalytic activity between $InTaO_4$ and $InNbO_4$ is mainly due to that conduction band levels formed by Ta 5d in TaO_6 and Nb 4d in NbO_6.

Dependence of the photocatalytic activity on irradiation wavelengths (λ) was measured under the light irradiation using different cut-off filters from full arc up to $\lambda = 600$ nm. As a comparison, dependence of TiO_2 photocatalyst (P25) was also measured using the same method. The results are plotted in Fig. 19. All samples were loaded with Pt particle co-catalyst. Dependence of the photocatalytic activity on irradiation wavelengths (λ) shows a normal photocatalyst behavior, with prolonging irradiation wavelength, the photocatalytic activity decreases rapidly. An obvious photocatalytic activity was observed when irradiated with a visible light ($\lambda > 420$ nm) was irradiated, showing that $InMO_4$ (M = V, Nb, Ta) can evolve hydrogen from CH_3OH/H_2O solution under visible light irradiation. The photocatalytic activity on $InVO_4$ was also obtained when a cut-off filter of $\lambda > 550$ nm was employed. However, the activity was disappeared when the irradiation wavelength was larger than 600 nm. This means that light response in photocatalytic activity occurred only at wavelengths shorter than 600 nm. The results are in good agreement with observation of UV-visible diffuse reflectance spectra (see Fig. 18).

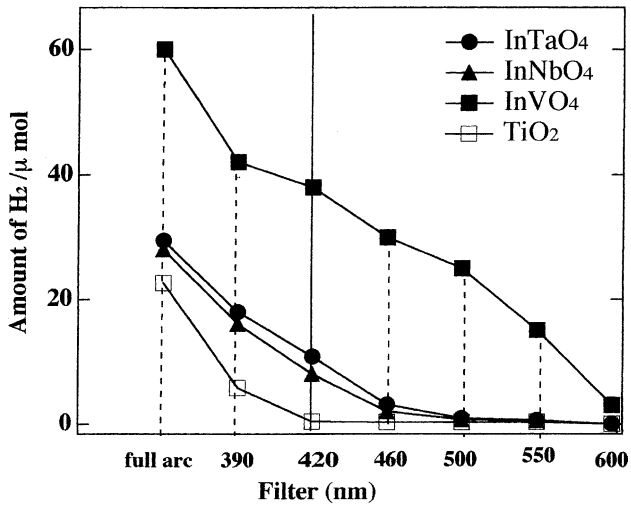

Fig. 19. Dependence of the photocatalytic activity of H_2 evolution from CH_3OH/H_2O solution over $Pt/InVO_4$, $Pt/InNbO_4$, $Pt/InTaO_4$ and Pt/TiO_2 on the wavelengths (λ) from full arc irradiation to $\lambda = 600$ nm.

The band structure of oxides is generally defined by d-level and O 2p-level, as confirmed by our theoretical calculations based on the first principles method for TiO_2 and $InTaO_4$ photocatalysts. Fig. 20(a) and (b) show the energy structure and density of states (DOS) of the TiO_2 photocatalyst in rutile structure. Fig. 20(c) shows the DOS of the new photocatalyst $InTaO_4$. The electronic structures were calculated using density functional theory (DFT) within the local density approximation (LDA) approach [34,36,37]. The common feature of the two oxide semiconductors is that the conduction band consists of mainly d orbital of the transition metal (3d of titanium in TiO_2, and 5d of tantalum in $InTaO_4$), and the valence band is spanned dominantly by 2p orbital of oxygen, which is shown with a dotted line.

For oxides with partly filled d-levels, the relationship between the flat band potential and the band gap can be described as $V_{fb}(\mathrm{SHE}) = 2.94 - E_g$, where V_{fb} is a flat band potential and E_g the band gap. Scaife [22] examined the band structure of the oxide $SrNb_2O_6$, which contains the NbO_6 octahedra, using the above rule. The valence band energy is at 2.94 (SHE), and the conduction band is at −0.7 (SHE) detected by the empty Nb d-levels. However, for oxides containing two kinds of octahedra such as $NiNb_2O_6$, Scaife found that the valence band energy should be assumed from both O 2p-levels of the NiO_6 and NbO_6 octahedra, and showed a value about 1 eV negative than 2.94 (SHE) of O 2p-levels. The conduction band was determined at −0.7 eV by d-levels of NbO_6, the lowest empty band. We speculate that the same case takes place in our newly developed $InMO_4$ (M = V, Nb, Ta) compounds since all these compounds contain two kinds of polyhedra, InO_6 and $NbO_6(TaO_6)$, or VO_4. From the observed parameters, it appears that $InNbO_4$ has $E_g = 2.6$ eV, and conduction band is −0.7 eV. Then the valence band energy could be expected to be 1.9 (SHE), about 1.1 eV negative than that of the O 2p-levels. If we assume that the valence bands in the three new photocatalysts are similar, then the band structures of $InMO_4$ (M = V, Nb, Ta) as well as TiO_2 could be shown schematically in Fig. 21. The conduction bands of $InNbO_4$ and $InTaO_4$ consist of Nb 4d, and Ta 5d, respectively, while that of $InVO_4$ is V 3d. The difference of band gaps among $InVO_4$, $InNbO_4$ and $InTaO_4$ might be due to the difference in their conduction bands. This is consistent with the observation of their photocatalytic activities. In any case, the potentials of conduction band of $InVO_4$, $InNbO_4$ and $InTaO_4$ are more negative than that of the H_2 evolution, leading to H_2 evolution from pure water.

The investigation on structure found that the M–O–M bond angles in $InTaO_4$ expands slightly from those of $InNbO_4$. Xu et al. [27,28] has studied the conducting property of niobate compounds consisting of chains/layers of NbO_6 octahedron. They found that the formed $[NbO_3]_\infty$ chains favor the formation of a narrow conduction band

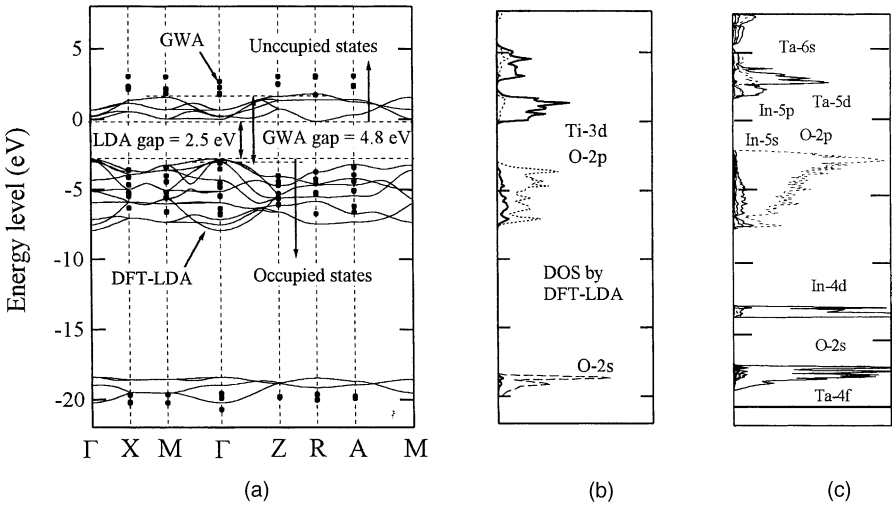

Fig. 20. A comparison of the electronic structures of TiO_2 and $InTaO_4$ [55].

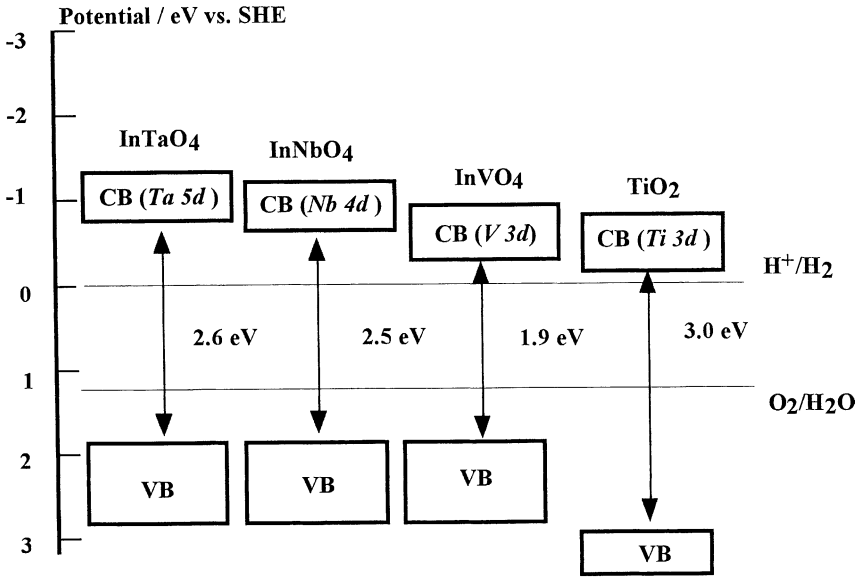

Fig. 21. Suggested band structures of $InTaO_4$, $InNbO_4$, $InVO_4$ and TiO_2 [55].

and a possible delocalization of the charge carriers. This is consistent with the relatively smaller resistivity in this direction. They also found that the 9° deviation of O–Nb–O angles from the ideal 90° is deleterious for conductivity. It appears that the electrons are trapped in narrow conduction bands and must be thermally activated to transport through the lattice. The study on influence of crystal structure on luminescent properties of tantalate and niobates showed that the closer the bond angle of M–O–M is to the ideal 180° the more the excitation energy is delocalized. This means that the bond angle of M–O–M is one of the important factors affecting the photocatalytic and photophysical properties of semiconductors. This suggests that although both of $InTaO_4$ and $InNbO_4$ have similar structure, photogenerated electron–hole pairs might move more easily in $InTaO_4$ than in $InNbO_4$. The mobility of electron–hole pairs affects the photocatalytic activity because it affects the probability of electron and hole to reach reaction sites on the surface of photocatalyst.

O_2 evolution reaction was performed in an aqueous silver nitrate solution under visible light irradiation ($\lambda > 420$ nm) and the following stoichiometric reaction took place:

$$4Ag^+ + 2H_2O \rightarrow 4Ag^0 + O_2 + 4H^+$$

The O_2 evolutions in the first 40 h increased rapidly. The formation rates of O_2 evolution were about 1 μmol g^{-1} h^{-1} for $InMO_4$ (M = Nb, Ta). This means that the photocatalysts have potentials for O_2 to evolve from aqueous solution and the photocatalytic activity for O_2 evolutions is almost the same.

Alig et al. [45] have shown that direct absorption of photons by band gap of oxides can generate electron–hole pairs in the solid. However, the energy of requirement to separate electron and hole in both conduction band and valence band is generally higher than the band gap of the oxides; that is in normal semiconductor the onset of absorption occurs at the $E_g + E_p(\omega)$ (E_p is the plus energy and ω the vibration frequency). Considering the fact that in the process of water splitting into H_2 and O_2 by photocatalysis, four holes and two electrons are necessary on surface of the photocatalysts at least. The process of photon absorption by photocatalyst might be imagined in Fig. 22. This is because the lowest-energy final state with zero momentum must contain two electron–hole pairs, each pair making an equal and opposite contribution to the total momentum. Even so, careful calculations predicted a soft rather than a sudden onset of absorption because zero momentum states of four particles should have a broad range of energies. This means that much larger energy than the band gap seems to be necessary to split water into H_2 and O_2 by photocatalysis. To remove the localized holes from the surface of photocatalysts, two ways are possible. The one is modification of the surface of the semiconductor particles, which may assist modification of the energy levels of the trapped holes. The other is direct increase of energy of light.

3.4. Metal doped $InTaO_4$ system

In order to improve photocatalytic activity of $InTaO_4$, we investigated the effect of substitution by 3d-metal (M) ions in $InTaO_4$. The significant effect of 3d M (M = Mn-$3d^5$, Fe-$3d^6$, Co-$3d^7$, Ni-$3d^8$, Cu-$3d^9$) ions in $In_{1-x}M_xTaO_4$ photocatalyst on the water splitting performance was observed [39,65,66]. The $InTaO_4$ photocatalyst has two kinds of octahedron in a unit cell, TaO_6 and InO_6. The volume of InO_6 octahedron in $InTaO_4$ is 13.601 $Å^3$. However, the volume of TaO_6 is 10.648 $Å^3$. This means that the volume of InO_6 octahedron was changed when with In being doped by M (M = Mn, Fe, Co, Ni, Cu) because the change of the M atomic radius, but crystal structure could not change. The change

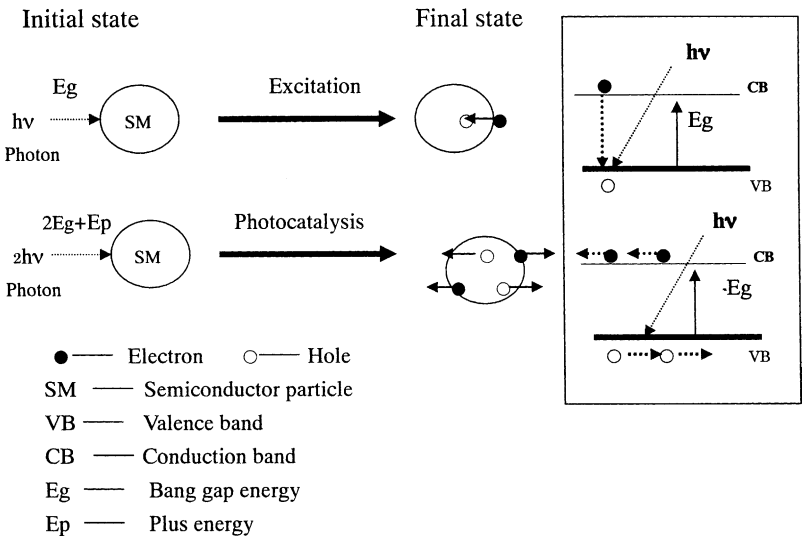

Fig. 22. The speculated process of absorption of a photon by photocatalyst.

of the InO_6 volume suggests leading to a slight change of the lattice parameters in the doped $InTaO_4$ system. We considered that M (M = Mn, Fe, Co, Ni, Cu) doping of $InTaO_4$ might cause a slight modification of crystal structure, that is, changes of lattice parameters such as bond lengths and bond angles, resulting in a change in photocatalytic property.

The crystal structure of the photocatalysts before and after photocatalytic reactions was investigated using X-ray powder diffraction. The result is shown in Fig. 23. The data were collected at 295 K with a step scan procedure in the range of 2θ = 5–100°. The step interval was 0.024° and scan speed was 1° min^{-1}. The powder X-ray diffraction analysis showed that all samples are the single phases. We could see that the Bragg peak distributions of the photocatalysts remain unchanged, indicating that the photocatalysts crystallize in the same crystal structure. Positional parameters and isotropic thermal parameters of the photocatalysts were refined. The result of refinement shows all the photocatalysts crystallize in the same wolframite structural type, monoclinic with space group P2/a.

The photocatalytic activity significantly changed with the variation of doping 3d M (M = Mn-3d[5], Fe-3d[6], Co-3d[7], Ni-3d[8], Cu-3d[9]) ions in $InTaO_4$. Fig. 24 shows the H_2 evolution from CH_3OH/H_2O solution under UV irradiation. The formation rates of H_2 were estimated to be 0.31, 0.08, 0.37,

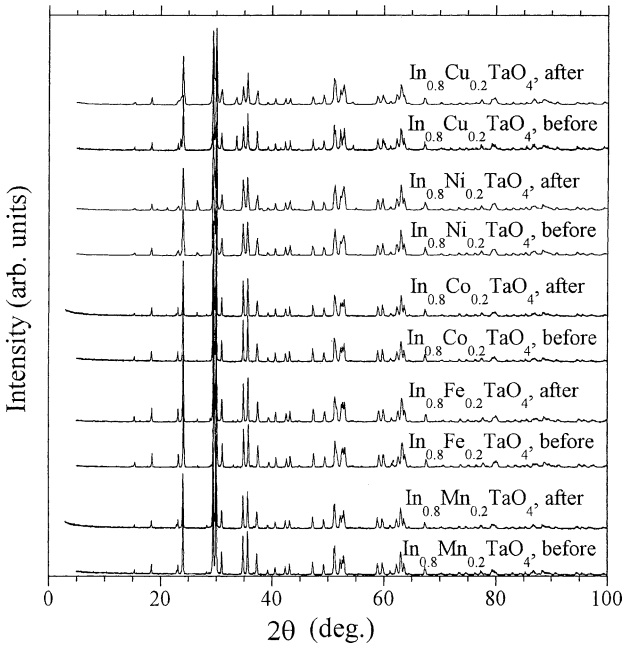

Fig. 23. X-ray powder diffraction patterns of photocatalysts before and after photocatalytic reaction.

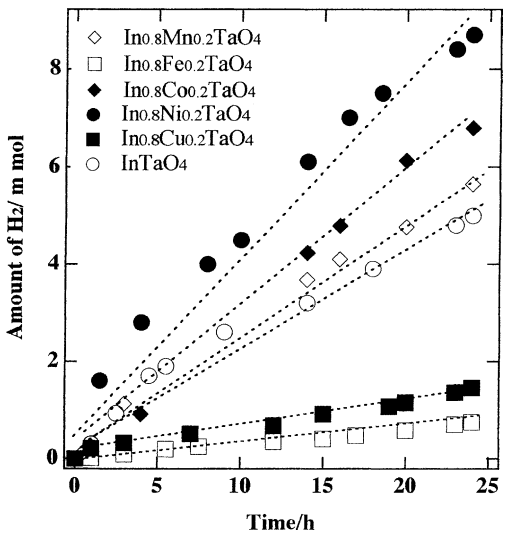

Fig. 24. Photocatalytic H_2 evolution on the $Pt/In_{0.8}M_{0.2}TaO_4$ (M = Mn, Fe, Co, Ni, Cu) compound from CH_3OH/H_2O solution under UV irradiation. Conditions: 0.5 g powder catalyst, 50 ml CH_3OH, 300 ml H_2O.

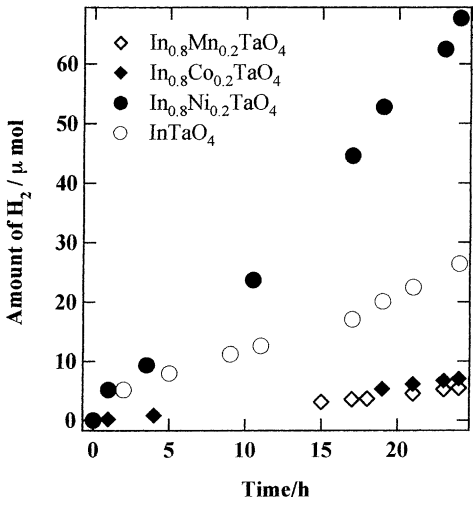

Fig. 25. Photocatalytic H_2 evolution using Pt/Mn-, Co- and Ni-doped $InTaO_4$ photocatalysts from CH_3OH/H_2O solution under visible light irradiation, Conditions: $\lambda > 420$ nm, a Pyrex glass cell, 300 W Xe arc lamp, 0.5 g powder catalyst, 50 ml CH_3OH, 200 ml H_2O.

0.47 and 0.1 mmol h^{-1} in the first 10 h for Mn, Fe, Co, Ni and Cu, respectively. The amount of evolved H_2 (mol) exceeded the amount of catalyst (about 1.38 mmol) at 24 h, indicating that the reaction occurs catalytically. The reaction stopped when the light was turned off in this experiment, showing the obvious light response. The result shows that the photocatalytic reaction is induced by the absorption of UV irradiation. The formation rate of H_2 increased on Mn, Co and Ni-doped $InTaO_4$, but decreased on the Cu and Fe-doped $InTaO_4$ photocatalysts compared with that of non-doped $InTaO_4$. The formation rate of H_2 on $In_{0.8}Ni_{0.2}TaO_4$ is about 180% than that of non-doped $InTaO_4$. The CO evolution as the oxidation product was observed in this reaction from CH_3OH/H_2O solution and it increases with illumination time, as does H_2 evolution. However, the rate of CO evolutions is much lower than that of H_2 evolution. The formation rate of CO changed with the variation of doping atoms, showing the same tendency as observed in H_2 evolution.

Under visible light irradiation ($\lambda > 420$ nm) H_2 and O_2 evolved from CH_3OH/H_2O and $AgNO_3/H_2O$ solutions, respectively, using the Mn, Co and Ni-doped $InTaO_4$ photocatalysts. The Cu and Fe-doped $InTaO_4$ photocatalysts cannot work at same conditions. Fig. 25 shows the H_2 evolution from CH_3OH/H_2O solution under visible light irradiation using Mn, Co and Ni-doped $InTaO_4$ photocatalysts. The H_2 evolution increased with illumination time. The formation rate of H_2 on Ni-doped $InTaO_4$ is much higher than that of the non-doped $InTaO_4$ photocatalyst, as does H_2 evolution under UV irradiation. The CO evolution was observed in this reaction from CH_3OH/H_2O solution as the oxidation product. However, the formation rates of H_2 on Mn and Co-doped $InTaO_4$ are much lower than that of the non-doped $InTaO_4$ photocatalyst. The effect of visible light irradiation was investigated by dark experiment. The H_2 evolution stopped when light irradiation was terminated, showing the obvious visible light response.

O_2 evolution reaction was performed in an aqueous silver nitrate solution under visible light irradiation ($\lambda > 420$ nm). The rate of O_2 evolution increased with In being doped by Ni in the $InTaO_4$ photocatalyst. However, the rate of O_2 evolution decreased with In being doped by Mn and Co in the $InTaO_4$ photocatalyst, as does H_2 evolution under visible light irradiation. The rate of O_2 evolution on $In_{0.8}Ni_{0.2}TaO_4$ is 1.1 μmol h^{-1}. The activity increased by about 140% than that of non-doped $InTaO_4$. It is often observed that doping transition metals into photocatalysts such as TiO_2 decreases significantly the photocatalytic activities. However, such a suppression effect by doping was not predominant in the Ni-doped $InTaO_4$ photocatalyst. The activity of Ni-doped $InTaO_4$ increased under both UV and visible light irradiation, respectively.

Dependence of the photocatalytic activity on irradiation wavelengths (λ) was also measured under the light irradiation from full arc up to $\lambda = 550$ nm using different cut-off filters. It shows a normal photocatalyst behavior such as that the photocatalytic activity decreases rapidly, since the number of incident photon was decreased when a cut-off filter was used. An obvious photocatalytic activity was observed when irradiated with a visible light ($\lambda > 420$ nm) was irradiated, showing that Mn, Co and Ni-doped $InTaO_4$ photocatalysts can respond visible light irradiation. The photocatalytic activity was also obtained when a cut-off filter of $\lambda > 460$ nm was employed. However, the activity was disappeared when λ of light irradiation was larger than 540 nm. This means that light response occurred only at wavelengths shorter than 540 nm. The surface area of these photocatalysts is similar. Therefore, the difference between the band structures of doping atoms might lead to the different photocatalytic activity.

3.5. $NiO_x/In_{1-x}Ni_xTaO_4$ system

Very recently, we have reported a new series of photocatalysts, NiO_x or RuO_2-loaded oxide semiconductors, $In_{1-x}Ni_xTaO_4$ ($x = 0$–0.2), which induces direct splitting of pure water into stoichiometric amounts of oxygen and hydrogen under visible light irradiation [16,39]. The photocatalytic activity changed with the variation of x in $In_{1-x}Ni_xTaO_4$ and the photocatalyst at $x = 0.1$ showed the highest activity. Fig. 26 shows the H_2 and O_2 stoichiometric evolution from pure water with the $NiO_x/In_{0.9}Ni_{0.1}TaO_4$ photocatalyst suspension under visible light irradiation ($\lambda > 420$ nm). The rates of H_2 and O_2 evolution were about 16.6 and 8.3 μmol h^{-1}, respectively. The gas evolution stopped when the light was turned off, showing that the reaction is induced by the absorption of visible light. It is worth indicating that after evacuating the system, almost the same rate was reproduced in the second run. Since the reaction of photocatalysis occurs on the surface of photocatalyst, parameters in ruling conversion efficiency of solar water

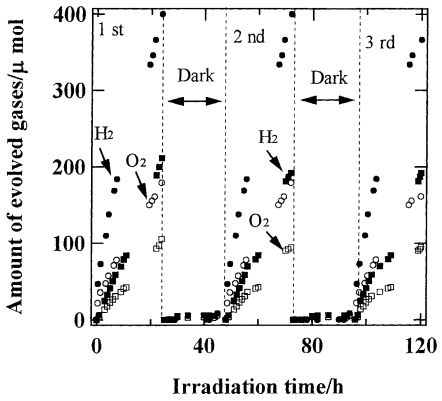

Fig. 26. Photocatalytic H_2 and O_2 evolutions from pure water on $NiO_y/In_{1-x}Ni_xTaO_4$ and $RuO_2/In_{1-x}Ni_xTaO_4$ ($x = 0$–0.2). Conditions: 0.5 g photocatalysts powder sample, 250 ml pure water in a Pyrex glass cell, visible light irradiation ($\lambda > 420$ nm), light source = 300 W Xe lamp.

splitting should include surface characteristics of photocatalyst. We examined the crystal structure and the characteristics of the surfaces of both semiconductor, $In_{0.9}Ni_{0.1}TaO_4$, and NiO_x-loaded $In_{0.9}Ni_{0.1}TaO_4$ photocatalyst.

XRD analysis showed that the change of the samples before and after reaction was unobservable. Full-profile structure refinement of XRD data was performed using the Rietveld program REITAN. The result shows all samples crystallize in the same wolframite structure, monoclinic with space group P2/a, but the lattice parameters decrease with increasing Ni along all the three axes in $x < 0.15$. Fig. 27 shows the change of V/Z with doping content, where V and Z are cell volume and the number of formulas per cell, respectively. The inset shows Ni dependence of c-axis, as an example of lattice parameter change. There is a linear decrease of V/Z as the Ni content in $x < 0.15$, while V/Z

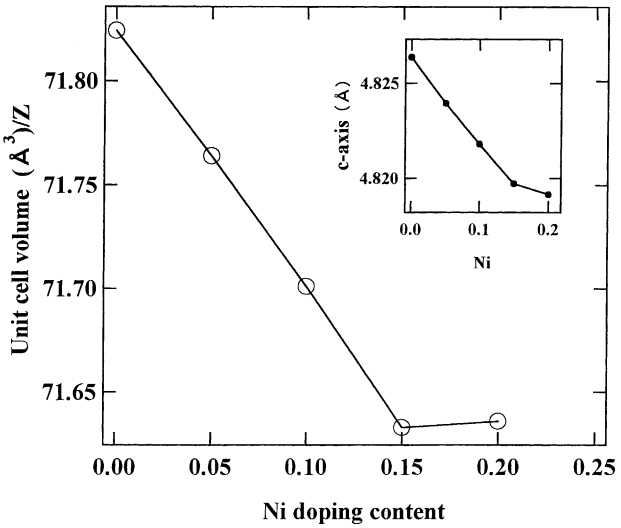

Fig. 27. The change of V/Z with doping content x, where V and Z are the cell volume and the number of formulas per cell, respectively. The inset shows Ni dependence of c-axis, as an example of lattice parameter change.

Fig. 28. TEM micrograph of the $In_{0.9}Ni_{0.1}TaO_4$ particles.

has a small expansion when the Ni content is $x > 0.15$. The structural stability of metal oxide consisting of octahedron, such as ABO_3, can be estimated by calculating the tolerance factor defined as $t = (r_A + r_0)/\sqrt{2}(r_B + r_0)$, where r_A, r_B and r_0 are the radii of the respective ions. The $0.79 < t < 1.1$ would be the ideal cubic structure. In this case, r_A is a maximum for radii of In and Ni. The t-value decreases with increasing x (Ni content), the t-value is <0.79 when $x > 0.15$, this suggests that the geometrical arrangement in the oxide governs the structural stability.

TEM–EDAX analysis shows that $In_{0.9}Ni_{0.1}TaO_4$ has a homogenous atomic distribution. The chemical composition is close to the starting stoichiometric amount of precursors. Fig. 28 shows the TEM micrograph of $In_{0.9}Ni_{0.1}TaO_4$. The fine particles with high crystallinity were observed. The particles with size in the range of 300–500 nm are dominant. It is known that the surface area affects the number of active sites in photocatalytic reaction of water splitting, and the particle size influences the distance that photogenerated electrons and holes have to migrate in the bulk of the semiconductor particle to reach the active sites. However, suppression of the recombination of the separated electron and hole excited by absorption of photon seems more important rather than both an increase in the surface area and a decrease in particle size. The high crystallinity and fineness of semiconductor particles might be efficient to suppress the

Fig. 29. TEM micrograph of $NiO_x/In_{0.9}Ni_{0.1}TaO_4$ photocatalyst.

recombination, resulting in an increase of conversion efficiency.

It is interesting to note that growth steps formed in the process of crystallization were observed clearly in the particle surface (see Fig. 28). The stage of the steps is about 3–5 nm. The step structure on the surface might contribute to yielding photocatalysis efficiency. But further investigation is necessary. In order to obtain higher photocatalytic activity, it is essential to load a metal or metal oxide on the surface of the semiconductor. We loaded 1 wt.% partly oxidized nickel as electron trap and H_2 evolution sites onto the $In_{0.9}Ni_{0.1}TaO_4$ surface. Fig. 29 shows the TEM micrograph of the $NiO_x/In_{0.9}Ni_{0.1}TaO_4$ photocatalyst. Nearly spherical NiO_x particles are distributed on the surface of $In_{0.9}Ni_{0.1}TaO_4$. EDAX analysis of the $NiO_x/In_{0.9}Ni_{0.1}TaO_4$ photocatalysts indicated that NiO_x is localized on the surface of the semiconductor $In_{0.9}Ni_{0.1}TaO_4$. The NiO_x particles with size of about 15 nm were localized on the surface of $In_{0.9}Ni_{0.1}TaO_4$. This system behaves as a short-circuited micro-photoelectrochemical cell.

The light absorption properties of $In_{1-x}Ni_xTaO_4$ were investigated as shown in Fig. 30. The visible absorption spectra of these compounds are extremely characteristic. This means that the photocatalysts have ability to respond to visible light. The band gap of these compounds can be estimated from plots of the square root of Kubelka–Munk

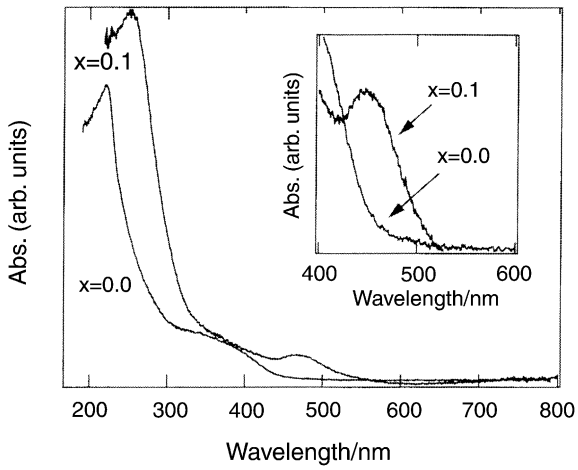

Fig. 30. UV-visible diffuse reflectance spectra of $In_{1-x}Ni_xTaO_4$ ($x = 0$ and 0.1) at room temperature. The inset shows UV-visible diffuse reflectance spectra of λ from 420 to 600 nm.

functions $F(R)$ vs. photon energy [20]. One of the most characteristic features is that the E_g is narrowed with Ni doping. The band gap is changed from 2.6 eV (non-doped) to 2.3 eV (0.1 Ni-doped). This is considered largely to be a consequence of the Ni-3d level [40]. The band structure of NiO might be assigned to Ni-$3d^8$ and Ni-$3d^9$. This suggests that the Ni-3d level forms a new energy level below the conduction band of $InTaO_4$. This is consistent with the observation from UV-visible spectra, which showed a broad absorption at 420–520 nm because of overlapping with another absorption. The phenomena might be attributed to internal transitions in a partly filled Ni-d shell. The narrower band gap suggests easier excitation for an electron from the valence band to the conduction band in oxide semiconductor. This results in higher photocatalytic activity.

Fig. 31 shows the speculated reaction mechanism. The surface of NiO_x is the cathode and the surface of $In_{0.9}Ni_{0.1}TaO_4$ is the anode. Band gap excitation in the bulk of the $In_{0.9}Ni_{0.1}TaO_4$ semiconductor injects electrons into the NiO_x particles and positively charged holes into the surface of the $In_{0.9}Ni_{0.1}TaO_4$ particles. Trapped electrons on the surface of NiO_x reduce water to hydrogen and the holes

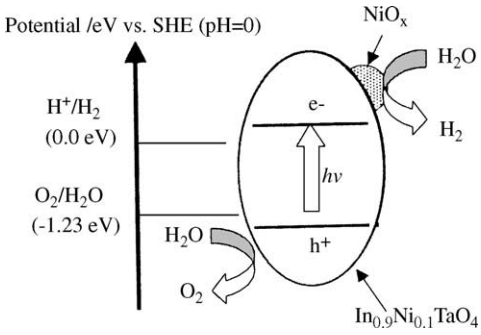

Fig. 31. Speculated reaction mechanism for the water splitting using $NiO_x/In_{0.9}Ni_{0.1}TaO_4$ photocatalyst.

on the surface of $In_{0.9}Ni_{0.1}TaO_4$ oxidize water to oxygen. The presence of NiO_x significantly enhances the H_2 and O_2 production.

4. Conclusion

We have presented the review of our research on photocatalytic splitting of water on newly synthesized photocatalysts. Our experimental results show that Bi_2MNbO_7 (M = Al, Ga, In, Y, rare earth) are sensitive to UV irradiation and that it is possible to obtain H_2 from both CH_3OH/H_2O solution and pure water. Although Bi_2MNbO_7 photocatalysts have a suitable band, the photocatalysts did not split pure water, even CH_3OH/H_2O solution under visible light irradiation to directly. Modification of the surface of the photocatalysts may be requested to increase responding wavelength range.

We have also presented the evidence for photocatalytic splitting of water with the $BiTa_{1-x}Nb_xO_4$ ($0 \leq x \leq 1$) photocatalysts. The change of x in $BiTa_{1-x}Nb_xO_4$ ($0 \leq x \leq 1$) could cause the change of structure. This difference of structure might cause the difference in the band levels and the corresponding difference in the band gaps, leading to different photocatalytic behavior.

Using $InTaO_4$ and $InNbO_4$ photocatalysts, we have firstly demonstrated the photocatalytic splitting of water in CH_3OH/H_2O solution under visible light irradiation. One of the most important key factors for $InTaO_4$ and $InNbO_4$ is that there are two kinds of octahedral, InO_6 and $NbO_6(TaO_6)$, in a unit cell for both of $InNbO_4$ and $InTaO_4$. The difference of volume between TaO_6 and NbO_6 leads to a change in lattice parameters between $InTaO_4$ and $InNbO_4$. Our experimental results show that the photocatalysts, M-doped $InTaO_4$ (M = Mn, Fe, Co, Ni and Cu) are sensitive to UV irradiation and that it is possible to obtain H_2 from an aqueous solution. Under visible light irradiation ($\lambda > 420$ nm) H_2 and O_2 were evolved using Mn, Co and Ni-doped and non-doped $InTaO_4$ photocatalyst from CH_3OH/H_2O and $AgNO_3/H_2O$ solutions, respectively. The $In_{0.8}Ni_{0.2}TaO_4$ photocatalyst showed much higher activity than that of the non-doped $InTaO_4$ photocatalyst. Ni-doped $InTaO_4$ has been developed as a new visible light photocatalysts for H_2 and O_2 evolutions from aqueous solutions. The study of doping effects on structural and photocatalytic properties of $InTaO_4$ solid oxide photocatalyst will provide useful information on the mechanism of the photocatalysts and also on making the stable photocatalysts with high activity under visible light irradiation.

Finally, we reported the direct splitting of pure water into stoichiometric H_2 and O_2 (mole ratio of $H_2/O_2 = 2$) under visible light irradiation ($\lambda > 420$ nm) using NiO_x (partly oxidized Ni) or RuO_2-loaded $In_{1-x}Ni_xTaO_4$ photocatalyst powder. We demonstrate efficient evolution of stoichiometric H_2/O_2 mixtures from pure water under visible light irradiation ($\lambda > 420$ nm) using these photocatalysts. The quantum was estimated to be 0.66% at light of 402 nm.

References

[1] B.S. Geoffrey, E.M. Thomas, J. Phys. Chem. B 101 (1997) 2508.
[2] K. Yeong, S. Samer, J.H. Munir, E.M. Thomas, J. Am. Chem. Soc. 113 (1991) 9561.
[3] K. Sayama, K. Yase, H. Arakawa, K. Asakura, K. Tanaka, K. Domen, T. Onishi, J. Photochem. Photobiol. A 114 (1998) 125.
[4] L.L. Amy, L. Guangqan, T. John, J.T. Yates Jr., Chem. Rev. 95 (1995) 735.
[5] T. Takata, A. Tanaka, M. Hara, J. Kodo, K. Domen, Catal. Today 44 (1998) 17.
[6] Z. Zou, J. Ye, H. Arakawa, Chem. Phys. Lett. 332 (2000) 271.
[7] Z. Zou, J. Ye, H. Arakawa, Chem. Phys. Lett. 333 (2001) 57.
[8] Z. Zou, J. Ye, K. Sayama, H. Arakawa, Chem. Phys. Lett. 343 (2001) 303.
[9] Z. Zou, J. Ye, R. Abe, H. Arakawa, Catal. Lett. 68 (2000) 235.
[10] T. Kawai, T. Sakata, Nature 286 (1980) 474.
[11] A. Kudo, H. Kato, Chem. Lett. (1997) 867.
[12] K. Honda, A. Fujishima, Nature 238 (1972) 37.
[13] H.G. Kim, D.W. Hwang, J. Kim, Y.G. Kim, J. Lee, Chem. Commun. (1999) 1077.
[14] A. Kudo, K. Omiori, H. Kato, J. Am. Chem. Soc. 121 (1999) 11459.
[15] A. Kudo, H. Kato, S. Nakagawa, J. Phys. Chem. B 104 (2000) 571.
[16] Z. Zou, J. Ye, K. Sayama, H. Arakawa, Nature 414 (2001) 625.
[17] Z. Zou, J. Ye, K. Oka, Y. Nishihara, Phys. Rev. Lett. 80 (1998) 1074.
[18] H.G. Kim, D.W. Hwang, J. Kim, Y.G. Kim, J. Lee, Chem. Commun. (1999) 1077.
[19] Z. Zou, J. Ye, H. Arakawa, Solid State Commun. 116 (2000) 259.
[20] Y. Kim, S. Atherton, E.S. Brigham, T.E. Mallouk, J. Phys. Chem. B 97 (1993) 11802.
[21] F. Izumi, J. Crystallogr. Assoc. Jpn. 27 (1985) 23.
[22] D.E. Scaife, Solar Energy 25 (1980) 41.
[23] H. Tada, A. Hattori, Y. Tokihisa, K. Imai, N. Tohee, S. Ito, J. Phys. Chem. B 104 (2000) 4585.
[24] M.P. Dare-Edwards, J.B. Goodenough, A. Hamnett, N.D. Nicholson, J. Chem. Soc., Faraday Trans. 2 77 (1981) 643.
[25] K. Yeong, S. Samer, J.H. Munir, E.M. Thomas, J. Am. Chem. Soc. 113 (1991) 9561.
[26] W. Monique, M. Wilma, B. George, J. Mater. Chem. 5 (1995) 981.
[27] J. Xu, T. Emge, V.K. Ramanujachary, P. Hohn, M. Greenblatt, J. Solid State Chem. 125 (1996) 192.
[28] J. Xu, M. Greenblatt, J. Solid State Chem. 121 (1996) 273.
[29] D. Lawless, N. Serpone, D. Meisel, J. Phys. Chem. 95 (1991) 5166.
[30] K. Vinodgopal, U. Staffors, K.A. Gray, P.V. Kamat, J. Phys. Chem. 98 (1994) 6797.
[31] R.C. Alig, S. Bloom, C.W. Struck, Phys. Rev. B 22 (1980) 5565.
[32] W. Gopel, G. Rocker, R. Feierabend, Phys. Rev. B 28 (1983) 3427.
[33] K.-I. Ishibashi, A. Fujishima, T. Watanabe, K. Hashimoto, J. Phys. Chem. B 104 (2000) 4934.
[34] T. Arima, Y. Tokura, Phys. Rev. B 48 (1993) 17006.
[35] S. Gregory, Phys. Rev. Lett. 39 (1977) 1035.
[36] K. Godehusen, T. Richter, P. Zimmermann, M. Martins, Phys. Rev. Lett. 88 (2002) 217601.
[37] T. Shibata, B. Bunker, J.F. Mitchell, P. Schiffer, Phys. Rev. Lett. 88 (2002) 207205.
[38] Z. Zou, J. Ye, H. Arakawa, J. Mater. Sci. Lett. 19 (2000) 1909.
[39] Z. Zou, J. Ye, H.J. Arakawa, Mater. Res. 17 (2002) 1419.
[40] M.P. Dare-Edwards, J.B. Goodenough, A. Hamnett, N.D. Nicholson, J. Chem. Soc., Faraday Trans. 77 (1981) 643.
[41] D. Lawless, N. Serpone, D. Meisel, J. Phys. Chem. 95 (1991) 5166.
[42] S. Goldstein, G. Czapski, J. Rabani, J. Phys. Chem. 98 (1994) 6586.
[43] Y. Yanagisawa, Y. Ota, Surf. Sci. 254 (1991) L433.
[44] G. Lu, L. Amy, J.T. Yates Jr., J. Chem. Phys. 102 (1995) 3005.
[45] J. Orensterin, Nature 401 (1999) 333.
[46] Y. Yanagisawa, Y. Ota, Surf. Sci. 245 (1991) 2433.
[47] S. Gregory, Phys. Rev. Lett. 40 (1978) 723.
[48] V. Cannella, J.A. Mydosh, Phys. Rev. B 6 (1972) 4220.

[49] J. Xu, T. Emge, V.K. Ramanujachary, P. Hohn, M. Greenblatt, J. Solid State Chem. 125 (1996) 192.
[50] K. Matsuura, T. Wada, T. Nakamizo, H. Yamauchi, S. Tanaka, J. Solid State Chem. 94 (1991) 294.
[51] D. Bernard, J. Pannetier, J. Lucas, Ferroelectrics 21 (1978) 429.
[52] G.I. Golovshchikove, V.A. Isupov, A.G. Tutov, A.G. Nikove, I.E. Myl, P.A. Nikitina, O.I. Tulinova, Sov. Phys. Solid State 14 (1973) 2539.
[53] Z. Zou, J. Ye, J. Alloys Comp. 292 (1999) 72.
[54] L.H. Brixner, H.Y. Chen, Mater. Res. Bull. 15 (1980) 607.
[55] J. Ye, Z. Zou, H. Arakawa, et al., J. Photochem. Photobiol. A 148 (2002) 79.
[56] Z. Zou, J. Ye, H. Arakawa, Chem. Mater. 13 (2001) 1765.
[57] Z. Zou, J. Ye, H. Arakawa, J. Mater. Res. 15 (2000) 2073.
[58] Z. Zou, J. Ye, H. Arakawa, J. Phys. Chem. B 106 (2002) 517.
[59] Z. Zou, J. Ye, H. Arakawa, J. Mater. Res. 16 (2001) 35.
[60] Z. Zou, J. Ye, H. Arakawa, J. Mol. Catal. A 168 (2001) 289.
[61] Z. Zou, J. Ye, H. Arakawa, Solid State Commun. 119 (2001) 471.
[62] Z. Zou, J. Ye, H. Arakawa, J. Mater. Res. 17 (2002) 1446.
[63] Z. Zou, J. Ye, H. Arakawa, Mater. Res. Bull. 36 (2001) 1185.
[64] J. Ye, Z. Zou, H. Arakawa, et al., Chem. Phys. Lett. 356 (2002) 221.
[65] Z. Zou, J. Ye, R. Abe, H. Arakawa, Catal. Lett. 75 (2001) 209.
[66] Z. Zou, J. Ye, R. Abe, H. Arakawa, J. Photochem. Photobiol. A 148 (2002) 65.